The LHCb RICH and Related Physics Topics

Jonas Rademacker
Univ. Oxford, NAPL, Keble Rd, Oxford, OX1 3RH, email: j.rademacker1@physics.ox.ac.uk
on behalf of the LHCb Collaboration

Abstract

After a short description of the relevant physics parameters for CP violation in the B system, and the LHCb detector, the LHCb RICH system is described in detail. The importance of the LHCb RICH for the LHCb physics programme is demonstrated, paying particular attention to the ability of LHCb to measure the CKM angle γ in many different channels.

1 Introduction

LHCb is a dedicated B–physics experiment at the future LHC collider, making use of the large number of B–hadrons expected at the LHC. The experiment is scheduled to start data taking in 2006. Crucial for the physics programme at LHCb, which focuses on precision measurements of CP violation parameters in many different B decay modes, is the RICH detector which provides particle identification.

Here we will give an overview of the LHCb RICH and its role in LHCb physics, focusing on one of the most attractive feature of LHCb, its ability to perform precision measurements on the CKM angle γ in many different decay channels, in both the $\mathrm{B_s^0}$ and the $\mathrm{B_d^0}$ system. This will thoroughly over constrain the Standard Model description of CP violation and provide a sensitive probe for New Physics.

2 CP Violation

2.1 CP Violation in the Standard Model

In the Standard Model, $\mathcal{CP}$ violation can be accommodated by a single complex phase δ_{13} in the CKM matrix, which is the matrix that relates the mass–eigenstates of the down–type quarks to the weak isospin partners of the up–type quarks:

$$V_{\mathrm{CKM}} = \begin{pmatrix} V_{ud} & V_{us} & V_{ub} \\ V_{cd} & V_{cs} & V_{cb} \\ V_{td} & V_{ts} & V_{tb} \end{pmatrix}. \tag{1}$$

The transition amplitude from a d to a u quark is proportional to V_{ud}, the transition amplitude from a u to a d quark to V_{ud}^*, etc.

The CKM matrix is closely related to the generation of fermion masses, the largest source of free parameters in the Standard Model. The only Standard Model prediction for this matrix is that it is unitary. Experimentally, it is found that the magnitudes of the CKM matrix elements follow a clear structure. In terms of the sine of the Cabibbo angle, $\lambda \equiv \sin\theta_C = 0.22$, the order of magnitude of the CKM matrix elements is:

$$\begin{pmatrix} 1 & \lambda & \lambda^3 \\ \lambda & 1 & \lambda^2 \\ \lambda^3 & \lambda^2 & 1 \end{pmatrix}. \tag{2}$$

Up to $\mathcal{O}(\lambda^3)$ in the Wolfenstein parametrisation of the CKM matrix [22], only the two smallest elements have complex phases (these phases are not independent and both would vanish if δ_{13} were 0):

$$V_{td} = |V_{td}|\, e^{-2i\beta} \qquad \text{and} \qquad V_{ub} = |V_{ub}|\, e^{-2i\gamma}. \tag{3}$$

Up to $\mathcal{O}(\lambda^3)$, β and γ are the only non-zero phases in the CKM matrix, and only decays involving $b \to u$ or $d \to t$ transitions can violate $\mathcal{CP}$. Both are accessible in the $\mathrm{B_d^0}$ system, and both can be measured at LHCb.

Figure 1: The CKM phases are observable as phase differences between interfering decay paths. For the examples of $B_d^0 \to J/\psi K_S$ and $B_d^0 \to \pi^+\pi^-$:

(a) $B_d^0 \to J/\psi K_S$ (b) $B_d^0 \to \pi^+\pi^-$

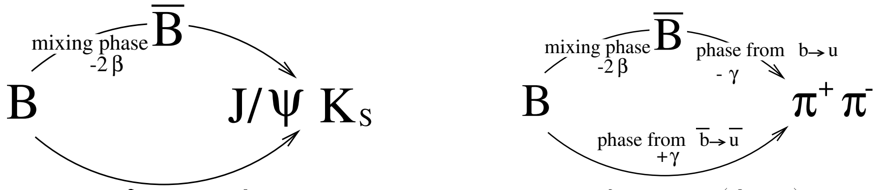

$\delta_{CP} = -2\beta$ $\delta_{CP} = -2(\beta + \gamma)$

2.2 β and γ in the B_d^0 System

2.2.1 The Angle β

The angle β appears via $V_{td} = |V_{td}|\, e^{-i\beta}$ in the box diagrams for B_d^0–$\overline{B_d^0}$ mixing:

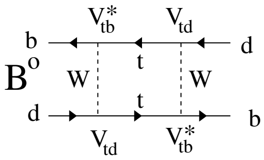

$\propto e^{-i2\beta}$ and

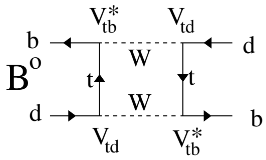

$\propto e^{-i2\beta}$. (4)

In principle, all up-type quarks (u, c, t) contribute to the internal quark lines; but since the amplitude is proportional to the mass of the internal quark, the top quark contribution dominates entirely.

The decay $B_d^0 \to J/\psi K_S$ is often referred to as the "gold–plated decay". It allows a clean extraction of the mixing angle 2β, as both the tree-level diagram and the penguin contribution to the decay have the same (zero) phase.

The mixing phase $\phi_{\rm mix} = -2\beta$ enters as the phase difference between the two interfering decay paths $B_d^0 \to J/\psi K_S$ with and without mixing, as illustrated in figure 1 (a). This phase difference can be observed in the time dependent decay rate asymmetry:

$$A(\tau) = \frac{\Gamma\left(B_d^0 \to J/\psi K_S\right) - \Gamma\left(\overline{B_d^0} \to J/\psi K_S\right)}{\Gamma\left(B_d^0 \to J/\psi K_S\right) + \Gamma\left(\overline{B_d^0} \to J/\psi K_S\right)} = \sin(2\beta)\sin(\Delta m\tau)\,, \tag{5}$$

where Δm is the mass difference between the two B_d^0 mass eigenstates and τ is the decay eigentime.

2.2.2 The Angle γ

The angle γ enters whenever a decay involves a $b \to u$ transition, the most prominent example being the decay to the $\mathcal{CP}$ eigenstate $\pi^+\pi^-$. Again, the measured quantity is the phase–difference between the two interfering decay paths, as illustrated in figure 1 (b). In the decay $B_d^0 \to \pi^+\pi^-$ this is, at tree-level, $2(\beta + \gamma)$. The time dependent asymmetry is:

$$A(\tau) = \sin(-2(\beta + \gamma))\sin(\Delta m\tau) \tag{6}$$

However, in interpreting the measured phase–difference as $2(\beta + \gamma)$, we have neglected penguin contributions, but here, in contrast to the case of $B_d^0 \to J/\psi K_S$, they do play a significant role. Several techniques have been proposed to measure the penguin contributions [14, 5], for example by combining this measurement with results from other, flavour-symmetry related decays [9]. Also, γ can be measured using decays like $B_d^0 \to D^{*-}\pi^+$ that do not involve penguin diagrams and therefore allow a theoretically clean extraction of the Standard Model γ.

2.3 The B_s^0 System

The LHC will not only produce a large number of B_d^0 mesons, it will also be a copious source of B_s^0 mesons. As the angle γ enters via $b \to u$ transitions, it is as accessible in the B_s^0 system as it is in the B_d^0 system, effectively doubling the number of potential decay channels to over-constrain γ. Having access to both the B_s^0 and the B_d^0 system also provides for a very promising way of constraining penguin contributions by combining the analysis of flavour–symmetry related decays, such as $B_d^0 \to \pi^+\pi^-$ and $B_s^0 \to K^+K^-$ [9].

The equivalent of the "gold plated" decay $B_d^0 \to J/\psi K_S$ in the B_d^0 system is the channel $B_s^0 \to J/\psi\phi$ in the B_s^0 system. It gives a clean measurement of the B_s^0–$\overline{B_s^0}$ mixing phase ϕ_{mix}^s. Up to $\mathcal{O}(\lambda^3)$ in the Wolfenstein parametrisation, this phase is zero. Finding a large mixing phase in the B_s^0 system would therefore be a sign of New Physics. Expanding the CKM matrix up to $\mathcal{O}(\lambda^4)$ introduces a small complex phase to V_{ts} of $\mathcal{O}(\lambda^2)$, referred to as $-\delta\gamma$. The B_s^0–$\overline{B_s^0}$ mixing phase in the Standard Model is therefore:

$$\phi_{\text{mix}}^s = -2\delta\gamma. \tag{7}$$

The measurement of γ, $\delta\gamma$ and other parameters in the B_s^0 system requires sensitivity to the very rapid B_s^0 oscillation period of $< 0.44\,\text{ps}$.

2.4 Entry Points for New Physics

The Standard Model is very predictive with respect to $\mathcal{CP}$ violation, which it parametrises with a single complex phase. This makes $\mathcal{CP}$ violation an ideal field to over–constrain the Standard Model and look for signs of New Physics.

Most extensions of the Standard Model are at high mass scales ($\gg M_W$). Significant effects at tree–level are therefore unlikely, but may enter as contributions to higher order processes. Those play an important role in many $\mathcal{CP}$ violation measurements in the B^0 systems. Two particular examples are B_d^0–$\overline{B_d^0}$ and B_s^0–$\overline{B_s^0}$ mixing which are mediated by box diagrams. Flavour Changing Neutral Currents, which appear in many New Physics models, could affect the mixing phase ϕ_{mix} (ϕ_{mix}^s) measured with $B_d^0 \to J/\psi K_S$ ($B_s^0 \to J/\psi\phi$), which is -2β ($-2\delta\gamma \approx 0$) in the Standard Model. For example, a significant mixing phase ϕ_{mix}^s in $B_s^0 \to J/\psi\phi$ would be a sign of New Physics.

Generally, since $\mathcal{CP}$ violation is an interference effect, higher order contributions due to New Physics can affect the measured phase–differences. This is true especially for those decays where loop-corrections are already important in the Standard Model. Decays with large penguin contributions are therefore particularly sensitive to New Physics, one example being $B_d^0 \to \pi^+\pi^-$.

One strategy pursued at LHCb for identifying New Physics contributions is to compare measurements of γ from channels that are more likely to be affected by New Physics, like $B_d^0 \to \pi^+\pi^-$, with results from channels that are expected to be robust against New Physics, like the penguin–free channel $B_d^0 \to D^*\pi$.

2.5 Status in 2006

By the year 2006, accurate measurements of $\sin(2\beta)$ are expected from the B^0 factories and the Tevatron. With $500\,\text{fb}^{-1}$ at the $\Upsilon(4S)$ and a similar performance from CDF and D$\emptyset$, the precision on $\sin(2\beta)$ is expected to be ~ 0.02.

Such a precision is not expected for the measurement of γ. The branching ratios of the relevant decay channels are either very small, typically $\mathcal{O}(10^{-5})$, or $\mathcal{CP}$ violating effects are tiny, as in $B_d^0 \to D^*\pi$, so very high statistics are required. The B_s^0 system that also allows measurements of γ is not accessible to the B^0-factories if they continue to run at the $\Upsilon(4S)$. While first estimates of γ might be possible, the uncertainties are expected to be too large to give strong constraints on the Standard Model description of $\mathcal{CP}$ violation.

Figure 2: The LHCb Detector shown in the bending (x-z) plane. The angular acceptance is 300 mrad.

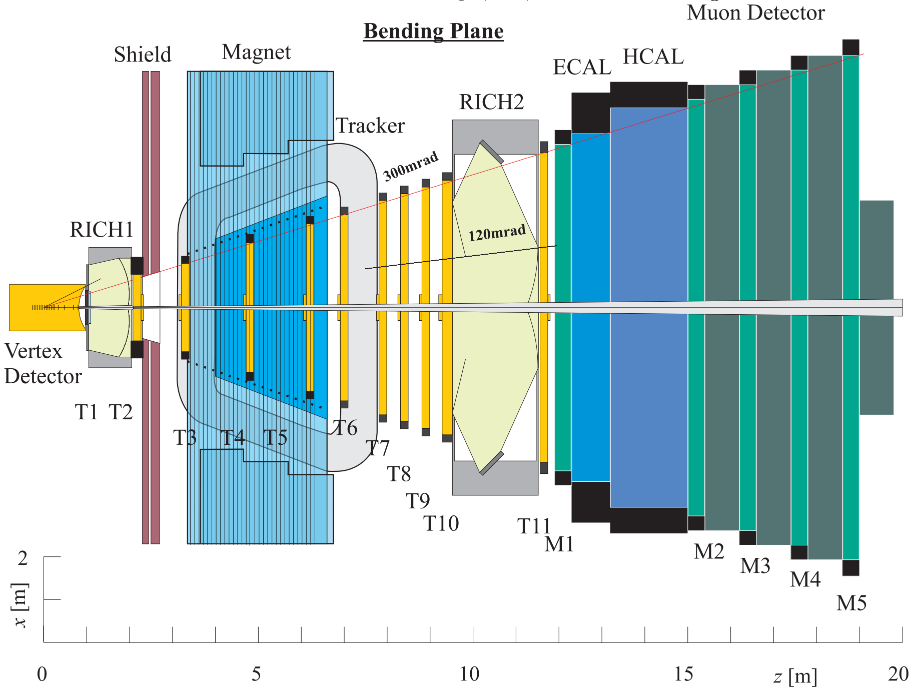

3 LHCb

3.1 LHC

The planned Large Hadron Collider (LHC) at CERN will collide protons at a centre–of–mass energy of 14 TeV at a design luminosity of $\sim 10^{34}\,\mathrm{cm}^{-1}\mathrm{s}^{-1}$. At these energies, direct observation of New Physics at mass–scales of ~ 1 TeV is feasible. The LHC will also be the most copious source of B hadrons in the world by several orders of magnitude.

The accelerator will be housed in the 27 km tunnel that has been built for the LEP experiment, that is presently being dismantled. LHC is scheduled to start data taking in 2006 with a luminosity of $10^{33}\,\mathrm{cm}^{-1}\mathrm{s}^{-1}$ and upgrade to its full luminosity after a few years. The high luminosity will be achieved by filling each of the two rings with 2835 bunches of 10^{11} particles each [15]; the interval between successive bunch crossings at each of the four interaction points is 25 ns.

3.2 LHCb

LHCb is specifically designed to make best use of the large number of $b\bar{b}$ pairs produced at the LHC. This large number is a consequence of the huge $b\bar{b}$ cross section for 14 TeV proton–proton collisions of $\sim 500\,\mu$barn [17]. The LHCb detector is a single arm spectrometer, which is motivated by the kinematics of $b\bar{b}$ production in high energy proton–proton collisions, as discussed below.

3.3 Bottom Production at LHCb

In proton–proton collisions, $b\bar{b}$ pairs are produced by flavour creation, flavour excitation and gluon splitting [17, 6]. A typical flavour creation mechanism, gluon fusion, is illustrated in figure 3 (a).

At LHC energies, the parton distribution functions of the proton are such that it is most likely that partons with very different momenta interact [6]. This has two major consequences for the design of a dedicated B physics detector:

Figure 3: B–hadrons at LHCb.

(a)Typical diagram for $b\bar{b}$ production in pp collisions [17].

(b) Momentum distribution for B^0_d mesons in $B^0_d \to \pi^+\pi^-$ decays [21].

(c) Polar angles of hadrons formed from $b\bar{b}$ pairs, calculated by PYTHIA [21].

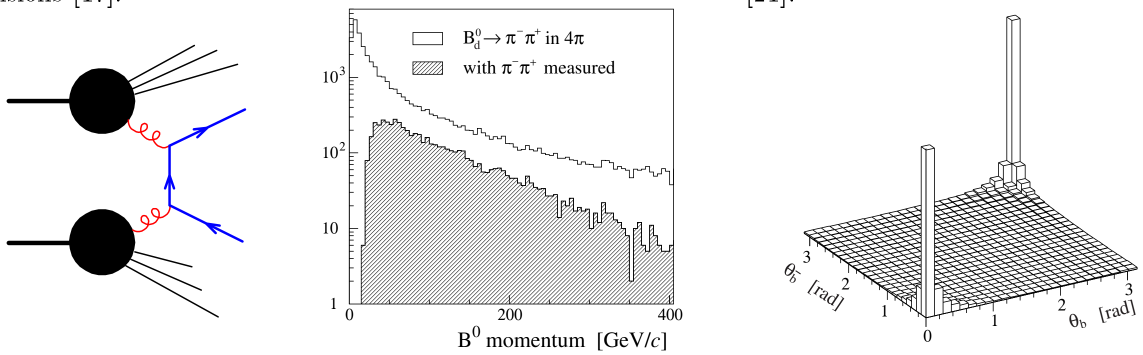

- The B hadrons produced are highly boosted, which results in long decay lengths ($\sim 1\,\mathrm{cm}$) and hence facilitates exact decay time measurements.
- Both the b and the $\bar{b}$, are predominantly produced in the same forward or backward cone, so that a single–arm spectrometer captures both B–hadrons produced, which is essential for B^0–tagging.

Momentum spectra of B^0_d mesons in $B^0_d \to \pi^+\pi^-$ decays are shown in figure 3 (b). The polar angle distribution of the $b\bar{b}$ pairs produced 14 TeV proton–proton collisions, simulated with PYTHIA is shown in figure 3 (c).

3.4 B^0–tagging

In order to measure the decay rate asymmetries, the flavour of the B^0–meson at the time of creation needs to be known. LHCb will predominantly use "opposite–side" tagging, where the flavour of the reconstructed B^0–meson at creation is estimated from the flavour of the accompanying B–hadron, (the "tagging B") at decay. The flavour of the tagging B is found by finding one particle that is likely to come from a B–decay, but does not come from the reconstructed B^0. This particle is either a lepton with high transverse momentum, or a kaon with high transverse momentum and significant impact parameter with respect to the primary vertex [21]. The charge of the lepton gives the charge and therefore the flavour of the b–quark it decayed from. Conversely, the charge of the tagging kaon is related to the flavour of the b quark via the decay chain $b \to c \to s$.

3.5 Luminosity

At the LHC design luminosity of $\sim 10^{34}\,\mathrm{cm}^{-1}\mathrm{s}^{-1}$, each bunch crossing would involve many inelastic proton–proton interaction. Such multiple interactions severely complicate the task of B^0–tagging, and of cleanly locating the primary and secondary vertices. Both are essential for measuring time dependent decay rate asymmetries.

Therefore the luminosity at the LHCb detector is reduced to $2 \cdot 10^{32}\,\mathrm{cm}^{-1}\mathrm{s}^{-1}$ by defocusing the beam at the LHCb interaction point. Remaining multiple–interaction events are rejected by the "pile–up veto counter", which is part of the vertex detector. Apart from optimising the number of single interactions, also the trigger performance, the detector occupancy and radiation levels are taken into account when choosing the design luminosity.

With this luminosity, LHCb expects about $5.6 \cdot 10^{11}$ single–interaction $b\bar{b}$ events passing the pile–up veto per year. Due to its comparably moderate luminosity requirements, LHCb can start its full physics programme from the first day of LHC running.

Figure 4: Invariant mass distributions for channels the measure the CKM angle γ, with same–topology background (simulation), without RICH [1].

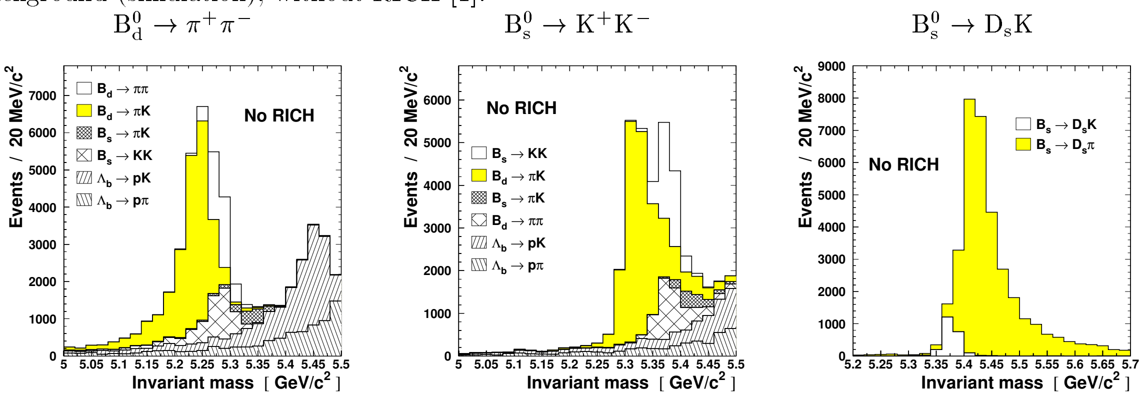

3.6 Detector Overview

Amongst the most important features of the the LHCb detector are:

- An excellent proper time resolution to exploit the full B physics potential at the LHC, including measurements in the rapidly oscillating B_s^0 system.
- Particle identification by two Ring Imaging CHerenkov (RICH) counters, for clean data samples and flavour tagging with kaons.
- A dedicated B trigger, including high p_t hadron and lifetime triggers for high efficiency.

Figure 2 shows a schematic overview of the LHCb detector. It comprises a vertex detector system, which includes the pile–up veto counter; a magnet and a tracking system; two RICH counters; an electromagnetic calorimeter and a hadron calorimeter, and a muon detector. All detector sub–systems, except for RICH 1, are split into two halves that can be separated horizontally for maintenance and access to the beam pipe.

4 The RICH system

4.1 Motivation

LHCb intends to perform high precision measurements in many different B decay channels. Many interesting decay channels are themselves backgrounds to topologically similar ones. Typically the branching ratios are of the order of $\sim 10^{-5}$. The particle identification and in particular K/π separation provided by the RICH is essential for a clean selection of decay channels involving the appropriate quark flavour and for tagging the B-hadron flavour with kaons. Figure 4 shows simulated invariant mass distributions for the channels $B_d^0 \to \pi^+\pi^-$, $B_d^0 \to \pi^+\pi^-$ and $B_s^0 \to D_sK$ [1], that allow measurements of γ. Also shown are background contributions from various same–topology decays. In all cases, the signal is overwhelmed by the background. The background channels can themselves show $\mathcal{CP}$ violation effects, which could cause uncontrollable systematic uncertainties at these low purities.

Also crucial for the measurement of decay–rate asymmetries is B^0–tagging, which is explained in section 3.4. The K/π separation provided by the RICH allows the use of kaons for B^0 tagging. This is equivalent to a $3\frac{1}{2}$ fold increase in statistics compared to the performance without kaon tagging. Figure 5 shows the momentum distribution of (a) pions in $B_d^0 \to \pi^+\pi^-$ events, and (b) tagging kaons. This illustrates the need for K/π separation over a wide range of momenta; LHCb seeks K/π separation from momenta of $\sim 1\,\mathrm{GeV}$ to beyond $100\,\mathrm{GeV}$.

Figure 5: Momentum distributions for (a) the highest momentum pion from $B_d^0 \to \pi^+\pi^-$, shown for momenta between 0 and 200 GeV, and (b) tagging kaons between 0 and 20 GeV [19].

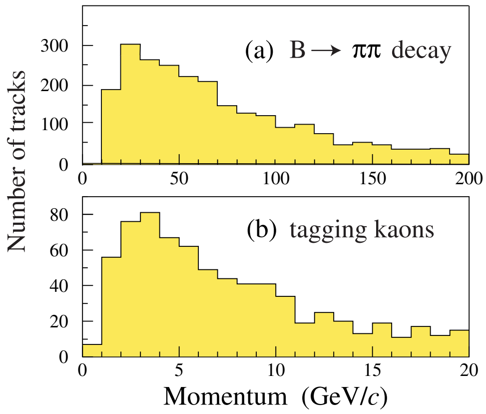

4.2 RICH Counters

RICH counters measure the opening angle θ_C of the Cherenkov cone by imaging it onto an array of photodetectors. Given the momentum p and the refractive index of the radiator medium, n, the mass m can be calculated from

$$\cos\theta_C = \frac{1}{n\beta} = \frac{1}{n}\sqrt{1 + \left(\frac{m}{p}\right)^2} \tag{8}$$

and the particle type can be identified.

4.2.1 Number of Detected Photons

The number of detected photons in a RICH counter is given by [10, 11, 23]:

$$N_{\text{p.e.}} \approx L\epsilon_A\epsilon_D \cdot \frac{370}{\text{eV cm}} \int Q(E)T(E)\sin^2\theta_C(E)\text{d}E. \tag{9}$$

where ϵ_A is the geometric efficiency of the detector, which is the probability that a photon reaching the photodetector plane hits the active area of a photodetector; L is the length of the radiator; $T(E)$ is the probability that a photon reaches the photo–detector plane, which comprises the transmission of the radiator gas, the mirror reflectivity, etc.; $Q(E)$ is the quantum efficiency of the photodetector; and ϵ_D is the efficiency with which the photo electron generated in the photo cathode is detected.

4.2.2 Resolution

The width of the Cherenkov angle distribution is determined by

- **Emission point error:** In the LHCb RICH, the spherical mirrors focussing the ring image onto the detector plane are slightly tilted relative to the beam direction, so that the point where a photon hits the detector surface depends on the position along the radiator where it was emitted, which is not known.
- **Chromatic dispersion:** The refractive index, and therefore the Cherenkov angle, depends on the wavelength of the emitted photon, which is not known.

- **Tracking:** To calculate θ_C from the hit position on the detector surface, the track direction needs to be known.
- **Pixelisation:** The photodetector granularity limits the position resolution on the detector plane, and therefore the Cherenkov angle resolution.

The Cherenkov angle resolution for the complete ring also depends on the

- **Number of photo electrons per track:** The more photo electrons are detected, the more accurate is the Cherenkov angle reconstruction. Assuming the errors on the Cherenkov angle reconstruction for each photon are independent, we get for the Cherenkov angle resolution of the whole ring: $\sigma_\theta \propto \frac{1}{\sqrt{N_{\mathrm{p.e.}}}}$.

4.2.3 Momentum Range

The lower end of the momentum range over which the RICH can operate is defined by the threshold for Cherenkov light emission:

$$\frac{1}{n}\sqrt{1+\left(\frac{m}{p}\right)^2} \leq 1 \Rightarrow p \geq \frac{m}{\sqrt{n^2-1}}. \tag{10}$$

For large momenta and small Cherenkov angles[1], the difference in Cherenkov angle for two particles of the same momentum, but different masses, is [18]:

$$\Delta\theta_c \approx -\frac{1}{2\sqrt{n^2-1}} \cdot \frac{\Delta(m^2)}{p^2}. \tag{11}$$

where, for K/π separation, $\Delta(m^2)$ the difference between the squares of the kaon and the pion mass: $\Delta(m^2) = m_K^2 - m_\pi^2 = 0.22\,\mathrm{GeV}^2$. The upper limit of the momentum range is therefore determined by the Cherenkov angle resolution σ_θ and the refractive index n of the radiator. Requiring n_σ sigma separation between the two particle hypotheses, the upper limit is given by:

$$p_{\mathsf{max}} \approx \sqrt{\frac{1}{2}\frac{1}{\sigma_\theta\sqrt{n^2-1}} \cdot \frac{\Delta(m^2)}{n_\sigma}}. \tag{12}$$

4.3 The LHCb RICH

4.3.1 Two RICH Detectors

As shown in equations 10 and 12, the upper and the lower limit of the momentum range covered by a RICH detector depend on the refractive index of the radiator, and the Cherenkov angle resolution. In order to provide K/π separation from $\sim 1\,\mathrm{GeV}$ to $> 100\,\mathrm{GeV}$, the LHCb RICH system employs two RICH detectors with three radiators.

The first radiator is silica aerogel with a refractive index of $n = 1.03$. This is suitable for the lowest momentum tracks starting at about 1 GeV. The useful wavelength range of the Cherenkov light emitted by the aerogel is limited by Rayleigh scattering of photons with small wavelength. The transmission of light of wavelength λ through a length L is proportional to e^{-CL/λ^4}, where C is the clarity coefficient. In the simulation studies for the assessment of the RICH performance, $C = 0.008\,\mu\mathrm{m}^4/\mathrm{cm}$ is assumed. Aerogels with $C = 0.004\,\mu\mathrm{m}^4/\mathrm{cm}$ are however under study, which would result in reduced photon losses due to scattering. A Mylar filter immediately downstream of the aerogel is used to absorb wavelengths below $\sim 350\,\mathrm{nm}$ in order to reduce the background due to scattered photons. The best possible efficiency for those unscattered photons transmitted by the mylar, extending into the visible spectrum, is an important consideration in the photodetector choice.

[1] The approximation of small angles is valid for the LHCb RICH system, where the maximum Cherenkov angle is between 32 mrad and 240 mrad (radiator dependent).

Figure 6: RICH 1[19].

(a) RICH 1 schematic (b) Rings in RICH 1

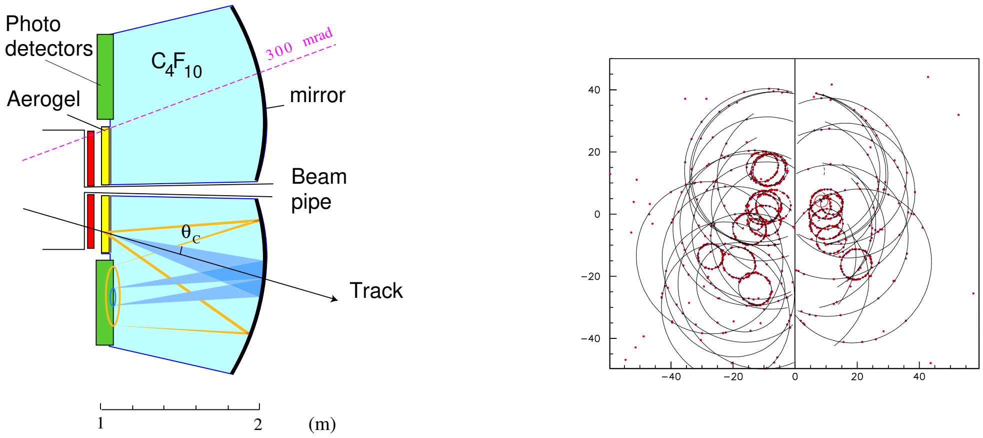

The intermediate momentum region is covered by gaseous C_4F_{10} with $n = 1.0014$, providing K/π separation up to $\sim 60\,$GeV. Both radiators are part of the **RICH 1** detector that is positioned close to the interaction region, immediately downstream of the vertex detector. This is to minimise the required photodetector area and to provide a wide acceptance for low-momentum particles. A schematic of RICH 1 is shown in figure 6 (a). RICH 1 covers tracks with polar angles between 25 and 300 mrad. The particle first traverses 5 cm of aerogel–radiator, and then 83 cm of C_4F_{10} gas. From simulation studies we expect to detect about 7 photons from the aerogel and 33 photons from the C_4F_{10} gas. Figure 6 (b) shows the two photo detector planes with (simulated) Cherenkov rings identified by the pattern recognition algorithm, and background. The rings from the aerogel and the gas are clearly visible and distinguishable.

In order to cover momenta up to $> 100\,$GeV and tracks at polar angles below 25 mrad, a second detector, **RICH 2**, is placed further downstream. Its polar angle acceptance starts at 15 mrad. Given the strong correlation between the momentum and the polar angle of the tracks, as demonstrated in figure 7 (a), it is sufficient for RICH 2 to cover polar angles up 120 mrad.

Equation 12 shows that, in order to increase the momentum coverage towards higher momenta, one can either improve the Cherenkov angle resolution, or reduce the refractive index. In RICH 2, both options are pursued. The radiator is CF_4 gas with $n = 1.0005$. To improve the resolution compared with RICH 1, a larger detector is constructed. The focal lengths of the mirror and mirror–detector distance are increased, which gives a larger image and thus reduces the pixelisation error. The small dispersion of CF_4 results in a reduced chromatic error. The smaller Cherenkov angle, and the reduced curvature of the mirror, lead to a reduced emission point error.

A schematic of RICH 2 is shown in figure 7 (b). In order to keep the length of the detector small, the light is reflected from the spherical mirrors first onto two flat mirrors, and from there to the detector plane.

4.4 Pattern Recognition

To associate rings in the two RICH detectors with tracks found in the tracking system and to make particle assignments, a global likelihood fit is performed, using all available information from the three radiators simultaneously. A likelihood function is optimised, assuming an approximately Gaussian shape for the Cherenkov angle distribution for each track, plus background. Figure 6 (b) shows rings in RICH 1, identified by the pattern recognition.

Figure 7: Polar angle vs. momentum, and RICH 2 schematic [19].

Polar angle versus momentum for all tracks in simulated $B_d^0 \to \pi^+\pi^-$ events.

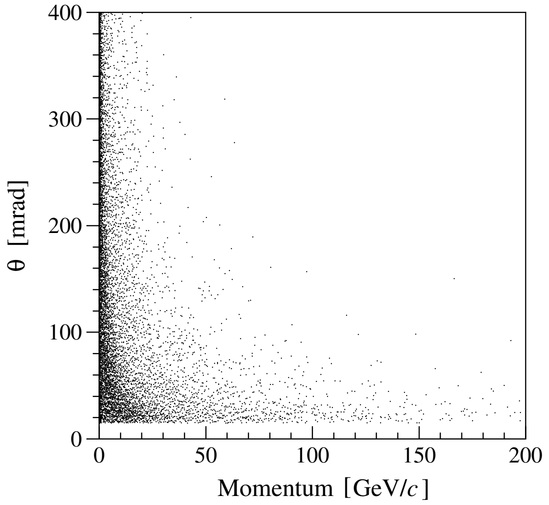

RICH 2 schematic, with RICH 1 drawn to scale for comparison

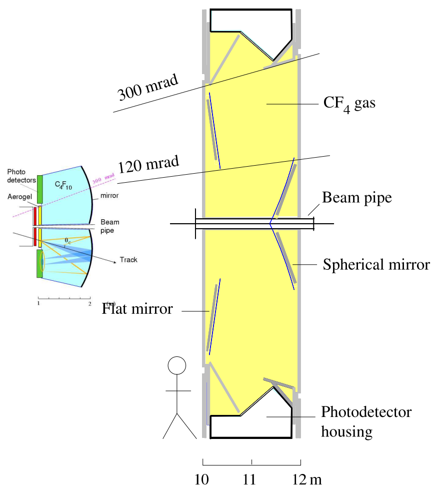

4.5 Photodetectors

The photodetector for the LHCb RICH must be efficient, with sensitivity extending into the visible spectrum; they must be fast enough to cope with the bunch–crossing frequency of 40 MHz; they need to be precise (pixel size: $\sim 2.5 \times 2.5\,\mathrm{mm}^2$) and affordable to cover $2.6\,\mathrm{m}^2$; they have to cope with radiation exposures up to 3 kRad/year; and need to be tolerant to magnetic fringe fields of $20 - 30$ gauss.

The baseline photodetector choice is the Pixel Hybrid Photo Diode (Pixel HPD) [12]. Multi–Anode Photo Multiplier Tubes [16] are kept as a back–up solution until all technical challenges of the HPDs have been solved.

4.6 The Pixel HPD

The HPD for the LHCb RICH detectors is being developed in association with the company DEP[2]. The HPD consists of a vacuum tube with a light–sensitive photo cathode at the entrance window and a silicon pixel detector at the tube base.

The sensitive range of the cathode extends approximately from 2 to 7 eV. The average quantum efficiency over this range is measured to be 15.4%, with a maximum of 28% at ~ 5 eV. These measurements include light losses in the entrance window.

Between the photocathode and the silicon detector a high voltage of 20 kV is applied. If a photon hitting the cathode is converted to an electron, this electron is accelerated by the applied electric field onto the Si sensor, where it creates $\sim 5 \cdot 10^3$ electron–hole pairs. The electrons released from the 75 mm diameter cathode are cross–focused by two electrodes onto the anode, demagnifying the image by a factor of ~ 5. To protect the electron optics from the residual magnetic field from the dipole magnet, each tube is enclosed in a cylindrical 0.9 mm thick μ–metal shield.

The Si sensor is bump–bonded to the binary readout chip; the whole anode assembly is enclosed in the tube. The anode is expected to detect the photo electrons with an efficiency of $\epsilon_D \approx 90\%$. The logical pixel–size on the anode is $500 \times 500\,\mu\mathrm{m}^2$, corresponding to an effective pixel size on the tube surface of $2.5 \times 2.5\,\mathrm{mm}^2$. A schematic of the tube with the μ–metal shield is shown in figure 8.

4.6.1 Occupancy and Binary Readout

Binary readout has the benefits of simplifying the electronics, reducing power consumption, and in particular reducing cost. The physics performance of the RICH will not be significantly affected by the

[2] Delft Electronische Producten (DEP), The Netherlands

Figure 8: Tube with μ–metal shield [19].

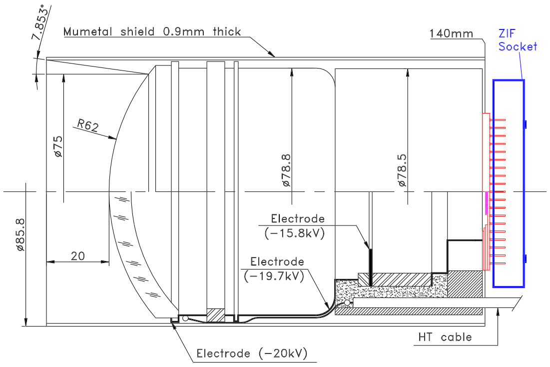

Table 1: Contributions (expressed in fractions of a radiation length) to the material in RICH 1 and RICH 2, which fall within the LHCb acceptance [19].

Item	RICH 1	RICH 2
Entrance window	0.001	0.014
Aerogel	0.033	
Gas radiator	0.024	0.017
Mirror	0.046	0.046
Mirror support	0.030	0.033
Exit window	0.006	0.014
Total (X_0)	0.140	0.124

reduced information provided by binary readout, because the occupancy levels per pixel are expected to be low and multiple photo electron events are therefore rare. Simulation studies show that the typical occupancy per pixel is about 1%, and never exceeds 8% [19].

4.6.2 Tube Mounting

The tubes will be stacked hexagonally in a metal support structure, with a distance of 87 mm between the tube centres. With a packing fraction for hexagonal close packing of 90.7% and an active diameter of 75 mm, this gives an active–area fraction of $\epsilon_A = 67\%$.

4.7 Mirrors and Alignment

The mirrors need to cover a total area of $\sim 20\,\mathrm{m}^2$. The mirrors will be made from 6 mm glass, coated with 900 nm aluminium, which will be protected by a 200 nm quartz layer. The expected reflectivity is 90%, averaged over the relevant wavelength range.

The mirrors will be aligned first by an in–situ survey of all positions. The precision of this first alignment is expected to be better than 0.5 mrad in RICH 1 and 0.1 mrad in RICH 2. Once LHCb operates, a laser system will be employed to monitor changes in time. To achieve the final precision of better than 0.1 mrad, $\beta = 1$ tracks in the data will be used.

4.8 Material Budget

The total material placed in the detector acceptance by the RICH system amounts to $\sim 26\%$ of a radiation length. The contributions from the different RICH components to the material budget are given in table 1.

Figure 9: RICH 1 prototype with full–scale HPD prototype with 61 pixel Si sensor

(a) Setup (b) Event display

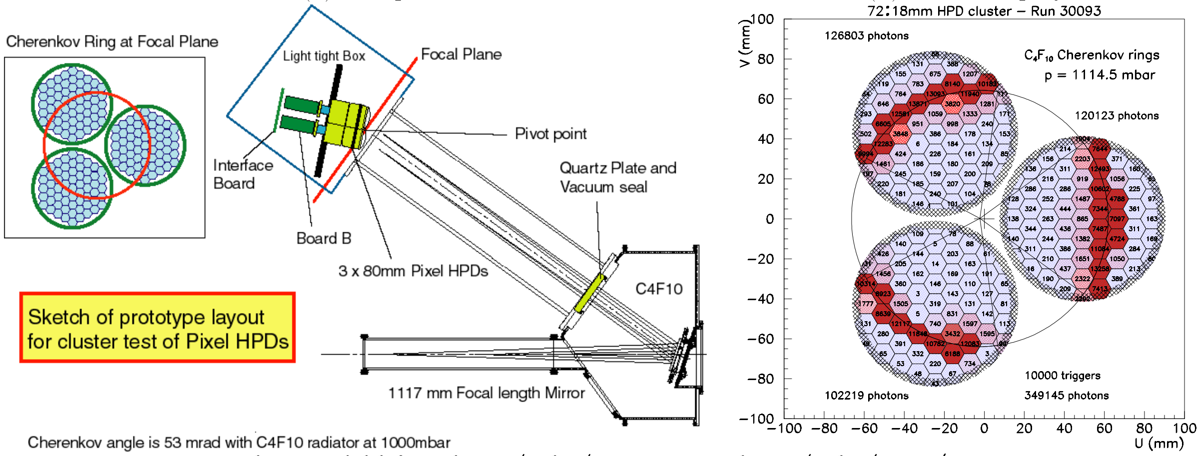

photon yield found: 7.7/tube/evt, expected: 7.8/tube/evt √

4.9 Prototype Tests

RICH prototypes with various setups and different photo detector technologies have been tested. The studies were carried out to confirm the performance of the detector elements and to validate the the computer model of the RICH used for the performance studies presented below.

4.9.1 RICH 1 prototype with full–scale pixel HPDs

A full–scale prototype of the RICH 1 detector was tested at the CERN SPS testbeam facility in summer 1999 [2, 4]. The detector was equipped with three pixel HPD prototypes. The pixel HPDs were identical to the final design except that the 1024–pixel Si sensor with binary read–out was replaced with a coarser 61–pixel sensor with analogue readout. A schematic of the setup is shown in figure 9 (a). Figure 9 (b) shows the photon counts per pixel, integrated over 10 000 events. The number of photo electrons per event found agrees very well with the number predicted from a detailed Monte Carlo simulation.

4.9.2 RICH 2 prototype with small 61–pixel HPD

A full–scale prototype of the RICH 2 prototype, equipped with commercially available, smaller, 61 pixel HPDs, was tested in 1998 [3]. The granularity of these tubes is comparable to that of the final design (hexagonal pixels with dimensions 2 mm flat to flat). The particle beam consisted of 50 GeV pions on and kaons. Figure 10 demonstrates the π/K separation of the RICH 2 detector. Photon counts and Cherenkov angle resolution agree well with the results of a detailed Monte Carlo simulation.

4.9.3 Electron Optics and Magnetic Fields

The electron optics cross–focus the photo electrons released from the 75 mm–diameter cathode onto a 15 mm–diameter area on the Si sensor. A full–scale prototype of the tube has been tested under different conditions [13] . This prototype differed from the final design in that it had a phosphor cathode, and a CCD camera instead of the pixel sensor for the photo electron detection.

No magnetic field: The tests show that the demagnification is almost perfectly linear across the cathode surface. The spatial resolution of the electron optics is described by the width of the Point Spread Function (PSF). The PSF describes the radial distribution of electrons on the Si surface, generated by a point source on the photo cathode. The width of the PSF is required to be much smaller than the pixel

Figure 10: π/K separation at 50 GeV in RICH 2 prototype

RICH 2 setup π/K separation

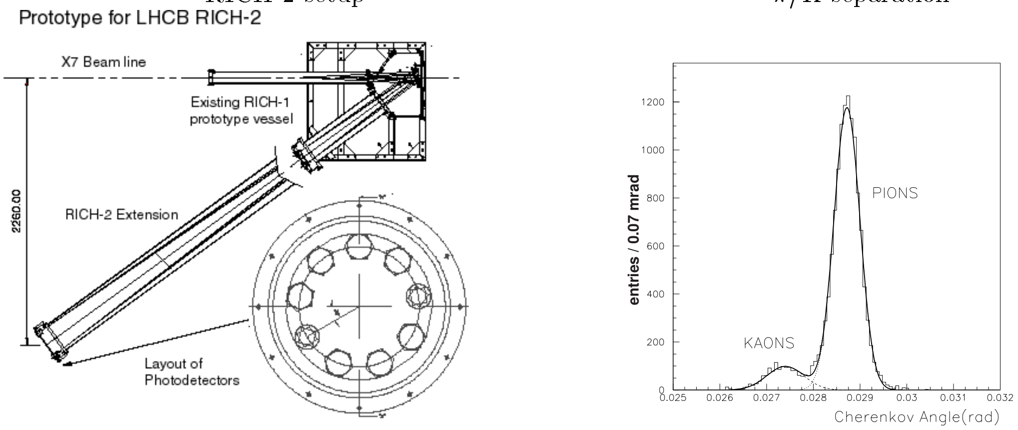

size on the Si sensor, which is $0.5 \times 0.5\,\mathrm{mm}^2$. In prototype tests, the RMS of the PSF was measured to be between 33 and 54 μm, clearly fulfilling this requirement.

With magnetic field: The prototype with fitted μ–metal shield has been tested in fields of up to 30 gauss. While a $\vec{\mathrm{B}}$ field perpendicular to the tube axis has only very little effect, it was found that a field of 30 gauss along the tube axis distorts the image on the Si detector significantly. However, the entire image remains on the Si sensor, and the point–spread function is not significantly affected. Hence the magnetic field effects can be corrected off–line.

4.9.4 Charged Particles

When charged particles traverse the tubes, Cherenkov light is generated in the entrance window of the tube. This light is detected by the photo detector and renders the corresponding pixels dead for genuine Cherenkov light from the radiators.

Tests with a full–scale prototype of the tube, equipped with a 61–pixel sensor, show that typically $25 - 35\,\%$ of a tube must be masked off when it is traversed by a particle. It is expected that these hits can be discriminated from genuine hits by the distinctive event shapes. From simulation studies and from tests in charged particle beams, it is expected that $10 - 15\,\%$ of all hits originate from charged–particles traversing the tubes.

4.10 LHCb RICH Performance

Table 2 summarises the characteristics of the three radiators of the RICH, and gives the values for the different contributions to the single–photon Cherenkov angle resolution, and the average number of detected photo electrons per ring. The values for σ_θ and $N_{\mathrm{p.e.}}$ are the result of a detailed simulation study [19].

Assuming for the Cherenkov angle resolution that $\sigma_\theta = \frac{\sigma_{\mathrm{single\ p.e.}}}{\sqrt{N_{\mathrm{p.e.}}}}$, we get a Cherenkov angle resolution for RICH 2 of 0.135 mrad. From equation 12 we obtain a 3σ K/π separation from ~ 1 GeV up to 93 GeV. A 2σ separation can be achieved up to 114 GeV, and 1σ up to 162 GeV.

Monte Carlo studies with a detailed model of the RICH and a full implementation of the pattern recognition algorithm have been performed. The results of the pattern recognition algorithm for the light particles e, μ, K and p are shown in table 3. The performance is given in terms of the purity $\mathcal{P}$ of the sample, and the efficiency ε. $\mathcal{P}$ is defined as the fraction of tracks for which a given RICH particle assignment is the correct; ε is defined as the fraction of tracks of a given type, that receive the correct particle assignment by the RICH. The table is given for well–reconstructed tracks with $1\,\mathrm{GeV} < p <$

Table 2: Characteristics of the 3 radiators

	RICH 2	RICH 1	
	CF_4	C_4F_{10}	Aero-gel
Characteristics			
L [cm]	167	85	5
n	1.0005	1.0014	1.03
$\theta_c^{\max}$ [mrad]	32	53	242
$p_{\mathrm{thresh}}(\pi)$ [GeV]	4.4	2.6	0.6
$p_{\mathrm{thresh}}(\mathrm{K})$ [GeV]	15.6	9.3	2.0
θ_c resolution for single photo electrons			
$\sigma_\theta^{\mathrm{emission}}$ [mrad]	0.31	0.74	0.60
$\sigma_\theta^{\mathrm{chromatic}}$ [mrad]	0.42	0.81	1.61
$\sigma_\theta^{\mathrm{pixel}}$ [mrad]	0.18	0.83	0.78
$\sigma_\theta^{\mathrm{track}}$ [mrad]	0.20	0.42	0.26
$\sigma_\theta^{\mathrm{total}}$ [mrad]	0.58	1.45	2.00
Number of photo electrons per ring			
N_{pe}	18.4	32.7	6.6

Table 3: Results from the pattern recognition applied to well–reconstructed tracks in triggered and accepted signal events between 1 and 150 GeV/c. Each track gives one entry in the table, and X denotes tracks below threshold in all radiators; the rows give the reconstructed particle type, $\mathcal{P}$ is the purity and ε the efficiency. The sample corresponds to 500k tracks, but has been normalised to 1000. From [19].

	True particle type						
Rec	e	μ	π	K	p	X	$\mathcal{P}$
e	97.4	0.7	24.6	1.4	0.5	3.1	0.76
μ	4.0	8.7	69.5	2.0	0.5	4.9	0.10
π	2.5	1.3	545.7	3.3	0.7	5.1	0.98
K	0.3	0.1	12.7	70.6	4.8	4.3	0.76
p	0.2	0.0	1.7	4.3	35.9	0.0	0.85
X	9.9	0.8	19.8	3.2	0.0	55.6	0.62
ε	0.85	0.76	0.81	0.83	0.85	0.76	

Figure 11: $B_d^0 \to \pi^+\pi^-$ and same–topology background, with and without RICH (simulation)

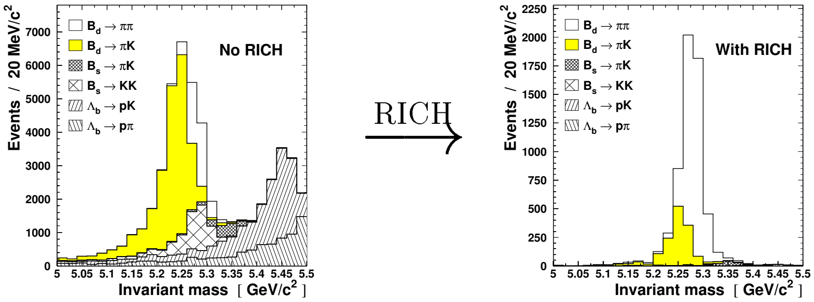

Figure 12: $B_s^0 \to K^+K^-$ and same–topology background, with and without RICH (simulation)

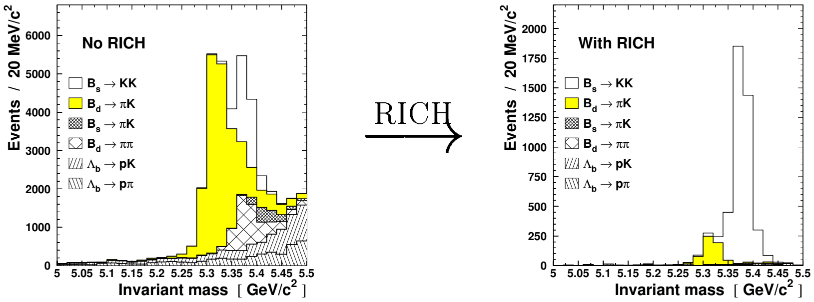

150 GeV. The K/π separation provided by the RICH is impressive: 95% of pions are identified as pions or lighter particles, and 92% of kaons as kaons or heavier particles.

4.11 RICH Physics

4.11.1 The RICH in Event Selection

Figures 11, 12, and 13 illustrate the dramatic improvements in the signal to background ratio that can be achieved by using the RICH, for three channels that measure the angle γ [1]. In all cases the efficiency of the signal selection is 80-90%.

Table 4 gives a few examples for decay channels that measure the CKM angle γ, with the expected precision on γ after one year of data taking. Most of the measurements listed in this table would be

Figure 13: $B_s^0 \to D_sK$ and same–topology background, with and without RICH (simulation)

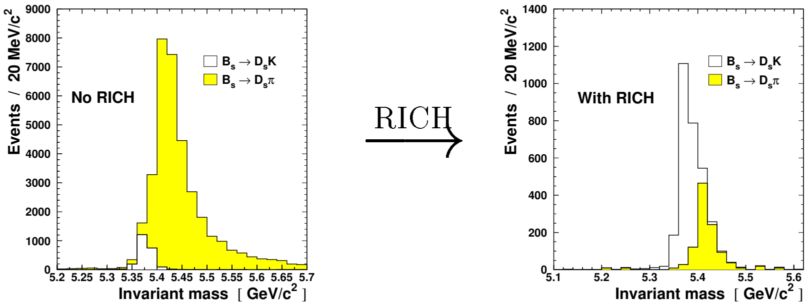

Table 4: Selected channels that are sensitive to γ. It is indicated whether they are likely to be affected by New Physics (NP) or not (SM). A estimate of the error on γ after one year of data taking is given [18, 5, 21].

Channel	SM	NP	σ_γ after 1 year
$B_d^0 \to D^{*\pm}\pi^{\mp}$	$\surd$		$\sim 7^\circ$
$B_s^0 \to D_s^{\pm}K^{\mp}$	$\surd$		$3^\circ - 13^\circ$
$B_d^0 \to \rho\pi$		$\surd$	$\sim 3^\circ$
$B_d^0 \to \pi^+\pi^-$, $B_s^0 \to K^+K^-$		$\surd$	$4^\circ - 8^\circ$
$B_d^0 \to D_d^+D_d^-$, $B_s^0 \to D_s^+D_s^-$		$\surd$	$\sim 3^\circ$

impossible without the K/π separation provided by the RICH. The γ reach estimates given in the table are approximate values, and are subject to different assumptions for certain physics parameters, especially on the frequency of the flavour–oscillation the B_s^0 system.

The channel $B_d^0 \to \rho\pi$ allows a theoretically clean extraction of both the tree and the penguin contributions [20]. The numbers for the channels $B_d^0 \to \pi\pi$ and $B_s^0 \to KK$ are given for a combined analysis. This allows to extract γ and the penguin contributions independently, assuming U–spin symmetry of the strong interaction [7]. The same method has been used for at the error estimate for the U-spin related pair $B_d^0 \to D_dD_d$ and $B_s^0 \to D_sD_s$ [8]. These channels would actually only measure the mixing angles 2β and $2\delta\gamma$, and not γ, if penguin contributions were small, so the entire "signal" is generated by penguins, which makes it particularly susceptible to New Physics.

In complete contrast to this are the channels $B_d^0 \to D^{*\pm}\pi^{\mp}$ and $B_s^0 \to D_s^{\pm}K^{\mp}$ where γ enters at tree level, and there are no penguin contributions. When compared with the former cases this will provide a very sensitive test of New Physics.

4.11.2 The RICH in B^0 Tagging

In order to decide the flavour of the reconstructed B^0 at its creation, LHCb uses electrons, muons and kaons from the decay of the accompanying B hadron (see section 3.4).

The kaon tag is only possible with the K/π separation provided by the RICH. The performance parameters of the kaon tag are [19]: efficiency $\epsilon = 31.2\%$, mistag rate $\omega = 31.0\%$. Hence the tagging power is $P_{\text{tag}} = 4.5\%$. The total tagging power at LHCb is $P_{\text{tag}} \approx 6.4\%$, therefore it can be seen that the kaon contribution is important.

5 Conclusion

When LHCb starts data taking in 2006, $\mathcal{CP}$ violation in the B_d^0 system is expected to be a well-established phenomenon, and the B_d^0–$\overline{B_d^0}$ mixing phase $\phi_{\text{mix}} = -2\beta$ will be precisely measured. Evidence for New Physics is in principle possible, for example in the case that ϕ_{mix} turns out to be near zero. However, meaningful constraints on the Standard Model from γ measurements are not expected.

LHCb will make use of the huge number of $b\bar{b}$ pairs created at the LHC to perform a comprehensive B–physics programme, that includes a significant improvement in the error on β, a measurement of $\delta\gamma$, and a number of precision measurements of γ in a variety of decay channels in both the B_d^0 and the B_s^0 system. One of the key features that facilitate this programme is the LHCb–RICH system. After one year of data taking, γ will be measured with a precision of a few degrees in many different decay channels, some sensitive to New Physics, while others are expected to be robust against New Physics. Comparing the results from those measurements will provide a sensitive probe of New Physics.

References

[1] M. Adinolfi, N. Brook, R. Forty, M. John, J. Libby, B. Simmons, and G. Wilkinson. A simulation study of the LHCb RICH performance. *LHCb Note*, 2001. LHCb 2000-066 RICH.

[2] E. Albrecht et al. *Nucl. Instr. and Meth.*, A 442:164, 2000.

[3] E. Albrecht et al. A prototype RICH detector using multi–anode photo multiplier tubes and hybrid photo–diodes. *LHCb 2000-68 RICH*, 2000. Submitted to Nucl. Instr. and Meth.

[4] M. Alemi et al. *IEEE Trans. Nucl. Sc.*, 46(6):1901, 1999.

[5] P. Ball et al. B decays at the LHC. In G. G. Altarelli and M. L. Mangano, editors, *1999 CERN Workshop on Standard Model Physics (and more) at the LHC, CERN, Geneva, Switzerland, 25 - 26 May 1999: Proceedings*, 2000. CERN 2000-004.

[6] Paolo Bartalini. Private communications, 2001.

[7] R. Fleischer. *Phys. Lett.*, B459:306, 1999.

[8] R. Fleischer. *Eur. Phys. J*, C10:299, 1999.

[9] Robert Fleischer. Constraining penguin contributions and the CKM angle γ through $\mathrm{B}_\mathrm{d}^0 \to \pi^+\pi^-$. *Eur. Phys. J.*, C16:87, 2000.

[10] I. M. Frank and I. E. Tamm. *Doklady AN SSSR*, 14:107, 1937.

[11] V. L. Ginzburg. *Zh. Eksp. Teor. Fiz*, 10:589, 608, 1940.

[12] T. Gys et al. The use of pixel hybrid photon detectors in the RICH counters of LHCb. *LHCb 2000-63 RICH*, 2000.

[13] T. Gys and D. Piedigrossi. Performance of full–scale pixel HPD tubes in low magntetic fields. *Nucl. Instr. and Meth.*, A 442:164, 2000.

[14] Harry J. Lipkin, Yosef Nir, Helen R. Quinn, and A. Snyder. Penguin trapping with isospin analysis and CP asymmetries in b decays. *Phys. Rev.*, D44:1454–1460, 1991.

[15] LHC - challenges in accelerator physics. http://lhc.web.cern.ch/lhc/general/gen_info.htm status: January 14, 1999.

[16] F. Muheim et al. Proposal for multi-anode photomultiplier tubes as photodetectors for the LHCb RICH. *LHCb 2000-65 RICH*, 2000.

[17] P. Nason et al. Bottom production. In G. G. Altarelli and M. L. Mangano, editors, *1999 CERN Workshop on Standard Model Physics (and more) at the LHC, CERN, Geneva, Switzerland, 25 - 26 May 1999: Proceedings*, 2000. CERN-2000-004.

[18] J. Rademacker. *Evaluation of the LHCb RICH Detectors and a Measurement of the CKM Angle γ*. PhD thesis, 2001.

[19] *LHCb RICH, Technical Design Report*, September 2000. CERN/LHCC/2000-0037.

[20] A. Snyder and H. R. Quinn. *Phys. Rev.*, D48:2139, 1993.

[21] *LHCb Technical Proposal*, February 1998. CERN/LHCC/98-4.

[22] Lincoln Wolfenstein. Parametrization of the Kobayashi-Maskawa matrix. *Phys. Rev. Lett.*, 51:1945, 1983.

[23] T. Ypsilantis and J. Seguinot. Theory of ring imaging Cherenkov counters. *Nuclear Instruments and Methods in Physics Research*, A 343:30–51, 1993.